Journal of Imaging Science and Technology® 53(3): 030501–030501-6, 2009.

Envelope Mapping Algorithm and Its Applications in Enhancement and Segmentation of Pancreatic Cell Images

Hai-Shan Wu, Mireille Bitar, David Burstein, Marie Ramer and Joan Gil
Department of Pathology, Box 1194, Mount Sinai School of Medicine, One Gustave L. Levy Place, New York, NY 10029
E-mail: haishan.wu@mssm.edu

Abstract. *In this paper, we present an intensity mapping algorithm for enhancement and segmentation of pancreatic ductal nuclei in pancreatic ductal cell images acquired from pancreatic fine needle aspiration specimens with Papanicolaou stain. The upper envelope surface is obtained by rolling a ball of fixed size on the image surface followed by a moving average filtering to smooth out the downward spikes. When the upper envelope surface is mapped to the uniform intensity of the maximum intensity of the original image, the contrasts inside nuclei are magnified and the difference between intensities in the cytoplasm regions and the void background is compressed, resulting in improved separation of the nuclei from the rest. Results of enhancement and segmentation of pancreatic nucleus images are provided and compared to those without envelope mapping.* © *2009 Society for Imaging Science and Technology.*
[DOI: 10.2352/J.ImagingSci.Technol.2009.53.3.030501]

INTRODUCTION

Carcinoma of the pancreas is the fifth most common cause of cancer related deaths in the Unites States. Most patients die within a year of diagnosis.[1] Fine needle aspiration (FNA) cytology[2] of the pancreas is often used because the relative nuclear changes are sometimes subtle, making it quite challenging to distinguish tumors such as adenocarcinoma of the pancreas from reactive ductal cells. Papanicolaou stain (Pap stain) is a polychromatic stain that allows the differentiation of cellular morphology, maturity, and metabolic activity and is the preferable method to enhance nuclear and chromatin details. In pathology, diagnoses of diseases are based on the recognition of visual clues or diagnostic criteria from the specimens. The enhancement of the nuclear contents is important since the enhanced images can reveal more and clearer details of nuclei for the viewing of pathologists.[3]

The main use of anatomic pathology is to secure the tissue diagnosis, in particular, the differential diagnosis between benign and malignant tumors.[4,5] The general approach used involves characterizing cells or nuclei with numerical measures of factors considered by pathologists based on visual estimate. A diagnosis is assigned on the basis of these features in accordance with a prescribed classificatory approach determined and validated on the basis of representative sets of cases. Among the most useful features for cytological applications have been measures of nuclear size, pleomorphism, and chromatin appearance.[4,6] To evaluate and identify the diagnostically important malignancy indicators from the microscopic cell images, segmentation of nuclei from the images is required so that the image analysis is performed only on the nuclei.[6–13]

The pancreatic cell images from FNA specimens stained by the Papanicolaou process usually have dark nuclei surrounded by lighter cytoplasm areas in a void background that is almost uniformly white. Considering the small size of nuclei against the large area including both nuclei and the surrounding cytoplasm, a very smooth surface that is tangent to the image surface should appear relatively flat in the nuclear regions. With an appropriate intensity mapping, we may enhance the contents in the dark nucleus regions without noticeable distortion while suppressing the difference in intensities between the cytoplasm and white background areas for the subsequent nuclear segmentation.

ENVELOPE MAPPING

A typical pancreatic cell image from a specimen stained by the Papanicolaou process consists of three parts. The first part consists of the nucleus regions with relatively lower average intensities. The second part is the cytoplasm areas that usually surround the nuclear regions. The cytoplasm area may appear slightly lighter on average in gray level than the nuclear regions. The third part is the void regions that have highest intensities since no stain occurs. [Figures 7(a) and 8(a) show two of the typical pancreatic cell images]. The nuclei, consisting of darker spots of nucleoli and chromatin clumps and whiter fillers, usually have sharp and wide fluctuating intensities, while the cytoplasm areas also fluctuate in intensities but in a slower pace.

Let a discrete pancreatic cell image of size $N_1 \times N_2$ be represented by $x(n_1, n_2)$, for $(n_1, n_2) \in D$, where the image domain $D = \{(n_1, n_2) \mid 0 \leq n_1 < N_1 \text{ and } 0 \leq n_2 < N_2\}$. The image x can be viewed as a surface for which the n_1 and n_2 coordinates represent the position and the gray-level x represents the height.[14] The envelope of an image is a pair of smooth surfaces that embrace the image. If the top envelope surface of x is represented by $\tilde{x}$, we have $x(n_1, n_2) \leq \tilde{x}(n_1, n_2)$ for $(n_1, n_2) \in D$. If we let a large ball roll over the surface of the cell image x, the lowest point of the ball will draw a surface above the image surface. The top envelope

Received Sep. 27, 2008; accepted for publication Feb. 14, 2009; published online Apr. 27, 2009.
1062-3701/2009/53(3)/030501/6/$20.00.

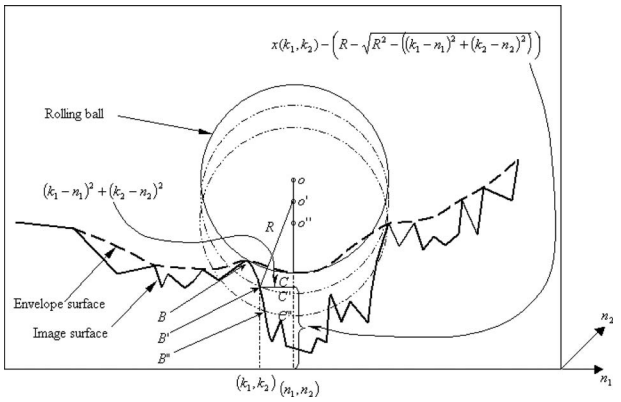

Figure 1. Schematic display of envelope surface in the dashed thick curve derived from a rolling ball of radius R along the top of the image surface in thick line. The rolling ball shown as a solid circle is tangent to the image surface, meaning that one or more image surface points are located exactly on the circle but none of them inside the circle.

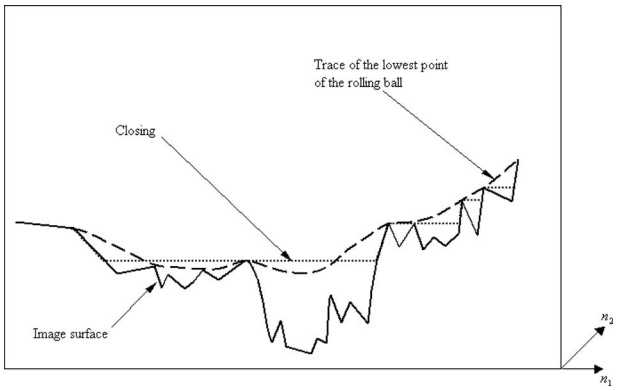

Figure 2. Comparison of the resulting envelope surfaces between the morphological closing (the dotted line) and the proposed algorithm (the dashed curve).

surface and the image surface are occasionally in touch. If the ball is chosen much larger than the nuclei, the nuclei, which usually have lower average intensities, will have little effect on the upper surface $\tilde{x}$. Referring to Figure 1, which shows a section along the n_1 axis, we let a large ball of radius R sit at the position (n_1,n_2). If a pixel at (k_1,k_2) is located in distance less than R from the center (n_1,n_2), we place a ball, centered at (n_1,n_2), to intersect with the image surface at $x(k_1,k_2)$. Fig. 1 shows three such balls, centered at o, o', and o'', intersecting with the image surface at B, B', and B'', respectively. The lowest points of the balls are at C, C', and C'', respectively. When intersecting the image surface at $x(k_1,k_2)$, the height of the lowest point of the ball centered at (n_1,n_2) is

$$c_{(n_1,n_2)}(k_1,k_2) = x(k_1,k_2) - \left(R - \sqrt{R^2 - ((k_1-n_1)^2 + (k_2-n_2)^2)}\right) \quad (1)$$

as shown the point marked as C' in Fig. 1. Since the ball that is tangent to the image surface (just in touch with the image surface but without any image surface inside the ball) as shown in the solid circle in Fig. 1 is the highest ball at (n_1,n_2), its bottom point marked by C in the figure is the highest for $\sqrt{((k_1-n_1)^2+(k_2-n_2)^2)} \leq R$. If we let the ball roll over the image surface, the C point will draw a surface that is above and touching the image surface such as

$$y(n_1,n_2) = \max_{(k_1,k_2)\in(D\cap D_{(n_2,n_2)})} c_{(n_1,n_2)}(k_1,k_2), \quad (2)$$

for $n_1=0,1,\ldots,N_1-1$, and $n_2=0,1,\ldots,N_2-1$, where the set

$$D_{(n_1,n_2)} = \{(k_1,k_2) \mid \sqrt{((k_1-n_1)^2+(k_2-n_2)^2)} \leq R\} \quad (3)$$

is a circular region centered at (n_1,n_2). The surface y is smooth at the local tops but may have sharp downward spikes at the local bottoms. To have a smooth envelope surface, we use a moving average filter that can smooth the downward spikes, while having little effect on the smooth areas of y at or near its local tops. Thus, we have the upper envelope surface of the image x as

$$\tilde{x}(n_1,n_2) = \frac{1}{N(n_1,n_2)} \sum\sum_{(k_1,k_2)\in(D\cap D_{(n_1,n_2)})} y(k_1,k_2), \quad \text{for } \forall\,(n_1,n_2) \in D, \quad (4)$$

where $N(n_1,n_2)$ is the number of elements in the set $D \cap D_{(n_1,n_2)}$.

Figure 2 illustrates the comparisons between the resulting envelope surface of the proposed algorithm and that of the closing operation, the cascade of the dilation that replaces each pixel with the brightest pixel in the R-pixel distance neighborhood and the erosion that replaces each pixel with the darkest pixel in the R-pixel distance neighborhood.[15–17] While the closing operation produces a line consisting of linear segments, the proposed algorithm yields a much smoother one that touches the image surface in more places.

To show the algorithm graphically, we display the simulated surfaces in one dimension in Figure 3. Fig. 3(a) shows an ideal signal in which the highest level on both ends stands for the bright background, the lowest level in center represents the nucleus region, and the rest represents the cytoplasm areas. Since images of natural scenes can often be described by the first-order Markov processes with the coefficients $0.9 \leq \rho < 1$,[18,19] we use the simulated signal, shown in Fig. 3(b), of the first-order Markov process generated by the first-order recursive system such as $y(n)=\rho y(n-1)+w(n)$, where $\rho=0.9$, w is the input, a white noise sequence, and y is the output sequence of the system; Fig. 3(c) is the simulated nucleus image in one dimension

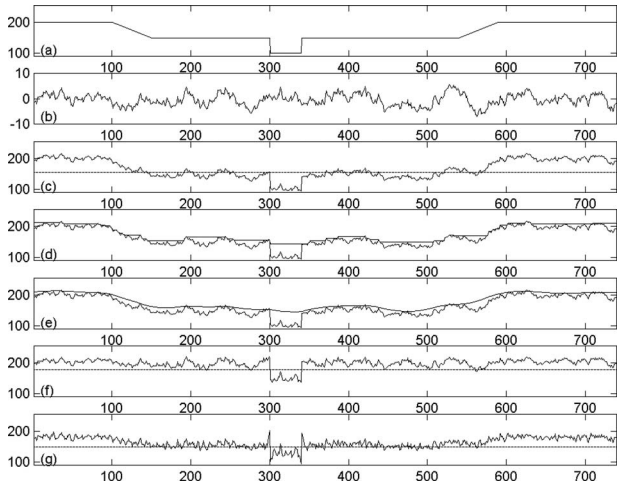

Figure 3. The envelope mapping algorithm illustrated by a simulated one-dimension cell signal. (a) the ideal one-dimensional signal; (b) the first-order Markov signal (ρ=0.9); (c) the simulated one-dimensional cell signal, constructed by the addition of the first-order Markov signal in (b) and the ideal signal in (a), and the supposed global threshold line that is the halfway of the intensity dynamic range; (d) the simulated signal with its morphological closing; (e) the simulated one-dimensional cell signal with the extracted upper envelope surface on top by the proposed enveloping algorithm; (f) mapped signal in solid line and the global threshold as the dashed line that is the halfway point of the dynamic range of the signal intensities (error rate 0.0148); and (g) homomorphic filtering result and the global threshold (dashed line) that is the halfway of the dynamic range of the signal intensities (error rate 0.1081).

that is the addition of the ideal signal in (a) and the first-order Markov process in Fig. 3(b). The dashed line in Fig. 3(c) is the middle of the intensity range simulating an automatic threshold

$$T_x = \tfrac{1}{2}(\max\{x(n_1,n_2)|(n_1,n_2) \in D\} + \min\{x(n_1,n_2)|(n_1,n_2) \in D\}), \quad (5)$$

where the functions max{·} and min{·} select the respective minimum and maximum elements from the sets. If we apply the automatic threshold T_x to the simulated original image x in (c), the large portion of the cytoplasm area below the dashed straight line will be misclassified as the nucleus pixels. Fig. 3(d) shows the simulated image x with its morphological closing on its top, while Fig. 3(e) shows the simulated image with the derived envelope surface $\tilde{x}$, a smooth line on the top of the image surface. An envelope mapping that drags the envelope intensities to the maximum intensity of the image x is given by

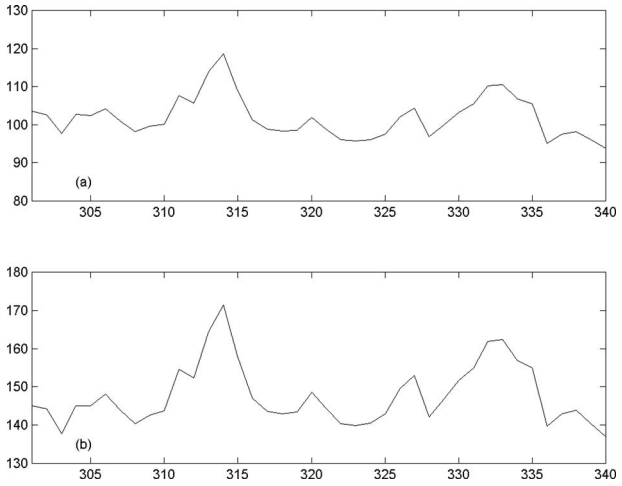

Figure 4. The simulated nucleus regions, both before and after the mapping to show the enhancement of the contents. The variance in the region is increased from 29.287 in (a) to 63.502 in (b) while the waveforms remain approximately identical because of the smoothness of the envelope surface based on which the intensity mapping is performed.

$$\tilde{x}(n_1,n_2) = \frac{\max\{\tilde{x}(k_1,k_2)|(k_1,k_2) \in D\}}{\tilde{x}(n_1,n_2)} x(n_1,n_2), \quad (6)$$

for $\forall(n_1,n_2) \in D$. The mapped image $\tilde{x}$ is shown in Fig. 3(f) along with the midthreshold

$$T_{\tilde{x}} = \tfrac{1}{2}(\max\{\tilde{x}(n_1,n_2)|(n_1,n_2) \in D\} + \min\{\tilde{x}(n_1,n_2)|(n_1,n_2) \in D\}) \quad (7)$$

in the leveled dashed line. As we can see, the intensities in cytoplasm regions are dragged to that of background, resulting in a more homogeneous combined background against the nucleus regions. There is a much smaller portion of the cytoplasm area crossing over the dashed threshold line, meaning smaller misclassification error after the envelope mapping. The error rate measured as the ratio of the number of the misclassified points to the total is 0.0149.

Homomorphic filtering, one type of Retinex algorithm, can produce simultaneous contrast enhancement and dynamic range reduction.[20,21] For the purpose of comparison, Fig. 3(g) shows the filtering result of the input signal in Fig. 3(c) by the homomorphic filter whose frequency response of the linear part is $H(\omega)=\gamma_l=0.5$ for $\omega \leqslant \omega_c-\Delta_w$, $H(\omega)=\gamma_r=2$ for $\omega \geqslant \omega_c+\Delta_w$, and linear $H(\omega)=\gamma_l+$

Table I. Enveloping algorithm versus homomorphic filtering in error rates.

Markov processes, ρ=0.9		1	2	3	4	5	6
Error rates	Enveloping	0.0108	0.0000	0.0027	0.0081	0.0054	0.0149
	Homomorphic filtering	0.1432	0.0649	0.2649	0.1608	0.1864	0.1351

$[(\omega-(\omega_c-\Delta_w))/2\Delta_w](\gamma_r-\gamma_i)$ for $\omega_c-\Delta_w<\omega\leqslant\omega_c+\Delta_w$, where $\omega_c=\pi/6$, and $\Delta_w=\omega_c/3$. The error rate from the homomorphic filtering is measured to be 0.1081, which is higher than 0.0149, the error rate from the proposed enveloping algorithm. Similar results from the enveloping algorithm and the homomorphic system on the six other randomly generated Markov processes are listed in Table I, showing that the enveloping algorithm performs better with lower errors.

Since the waveforms in the image x are fluctuating much quicker than the envelope $\tilde{x}$, a basically smooth surface, the waveforms are preserved with minimal distortions as shown in Figure 4, in which (a) shows the portion of the simulated nucleus area in Fig. 3(c) and 3(b), shows the corresponding area after the envelope mapping in Fig. 3(f). The variance, measured as

$$\frac{1}{M}\sum_{m=0}^{M-1} v^2(m)-\left(\frac{1}{M}\sum_{m=0}^{M-1} v(m)\right)^2,$$

where v is the discrete signal of length M, is increased from 29.287 in Fig. 4(a) to 63.502 in Fig. 4(b), while the waveforms remain approximately identical because of the smoothness of the envelope surface based on which the intensity mapping is performed. Thus, the contents inside the nuclei are magnified significantly without large distortions.

When images are enhanced by either homomorphic system or enveloping algorithm, distortions occur both inside and outside of cell regions. To compare the quality of the enhanced signals, we calculate the correlation coefficients between the input Markov processes and the output enhancements. Figure 5(a) shows the sample Markov process which appeared in Fig. 3(b); Fig. 5(b) shows the enveloping output signal from Fig. 3(f) with the class means removed, and Fig. 5(c) shows the homomorphic filtering result in Fig. 3(g) with the class means removed. The enveloping output signal appears more similar to the original than does the homomorphic result. The correlation coefficients are 0.8571 between the original signal in Fig. 5(a) and the enveloping output signal (class means removed) in Fig. 5(b), and 0.6007 between the original and the homomorphic filtering output (class means removed) in Fig. 5(c).

With the same input signals used for Table I, we compute the correlation coefficients between the input signals and each of the mean-neutralized outputs of the enveloping and homomorphic filtering systems and list them in Table II, which shows that the coefficients for the enveloping system are much higher, implying higher similarities and less distortions.

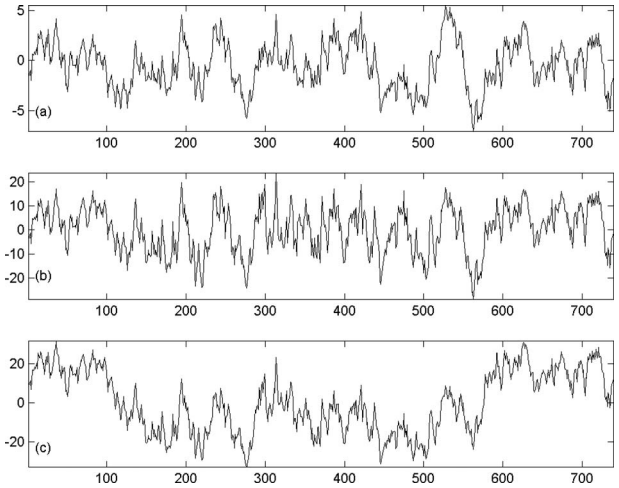

Figure 5. Similarities between the original and the enhanced signals. (a) Markov process, (b) the enveloping output signal (class means removed), and (c) homomorphic filtering result (class means removed).

RESULTS

We have applied the proposed algorithm to images of pancreatic ductal cells with Pap stain. Figure 6 displays two original color images of pancreatic ductal cells from specimens obtained via FNA-guided procedure and with Pap stain by a microscope with a lens of magnification 40×. The metric image dimension is $121.5\times92.1\ \mu^2$. Although the images are color stained, they do not have significant color variations. The blue component has a very narrow dynamic intensity range located at the high intensity end, while the green and blue components are very similar to each other, resulting in a bluish color image. For simplicity of computation and analysis, we apply the proposed algorithm on the gray-level images as shown in Figures 7(a) and 8(a). To preserve the waveforms inside nuclei, we wish the derived envelope to be smooth and leveled. Thus, the diameter of the rolling ball should be selected larger than the diameter of the nuclei in the image. In the images in Figs. 7 and 8, the diameters of nuclei are limited in the range between 20 and 50 pixels. Thus, we select the radius of the ball as 25, the high end of the radius range of nuclei. Fig. 7(b) displays the enhanced image of (a) by the envelope mapping that drags the intensities in the area of cytoplasm toward the bright background intensities resulting in whitened cytoplasm regions and higher contrasts inside nuclei. Fig. 7(c) shows the global thresholding segmentation of the image x in (a) with the automatic threshold, T_x, the middle of the dynamic image intensity range of x, while Fig. 7(d) shows the segmentation of $\tilde{x}$ by applying the automatic threshold, $T_{\tilde{x}}$, the middle value in the dynamic intensity range of the mapped

Table II. Correlation coefficients.

Markov processes, $\rho=0.9$		1	2	3	4	5	6
Correlation coefficients	Enveloping	0.8621	0.7709	0.8371	0.8286	0.8179	0.8208
	Homomorphic filtering	0.5798	0.4545	0.4680	0.6080	0.3481	0.5421

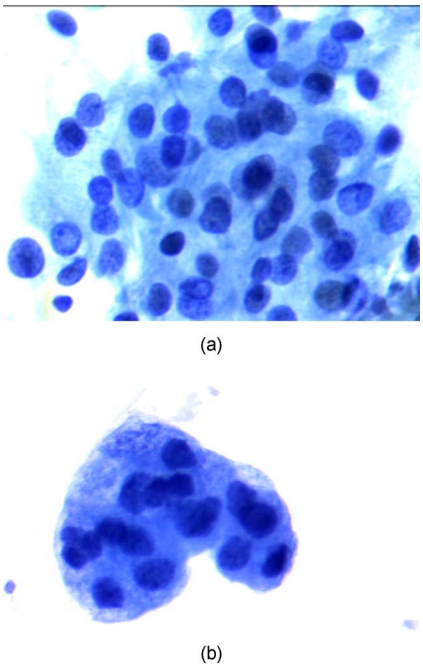

Figure 6. Original color images of pancreatic ductal cells. Images appear overwhelmingly blue since, in each image, the blue component has an almost uniform intensity at the high end, and the other two components are similar to each other. Both images contain malignant cells.

image $\tilde{x}$ in (b). It is observed that the segmentation has improved significantly, especially in the congested area where the cytoplasm intensities are relatively more uniform.

Fig. 8(a) shows another pancreatic cell image. Fig. 8(b) shows the enhanced image of (a) by the envelope mapping. Fig. 8(c) shows the global thresholding segmentation of the image in (a) with the automatic threshold, T_x, while image (d) shows the segmentation of envelope-mapped image in (b) by applying the automatic threshold, $T_{\tilde{x}}$. As we can see again, the segmentation has improved significantly in (d) and nuclear contents are enhanced greatly in (b).

Since the mapping algorithm assumes a very slow changing envelope on an image surface, the regions of the low intensities such as the regions formed by both the cytoplasm and the cells should be very large. The images of malignant cells usually have large cell clusters and thus are applicable to the proposed algorithm. Images of benign cases usually have cells in a very homogeneous distribution, therefore are relatively easier to be segmented with the global thresholding without a prior intensity equalization mapping.

CONCLUSIONS

We have presented an equalization mapping algorithm for enhancement and segmentation of pancreatic ductal nucleus images from FNA specimens with Papanicolaou stain. The algorithm assumes that clustered dark nuclei are embedded in large cytoplasm regions. Results for images of malignant pancreatic ductal cells show that the segmentations of nuclei with the proposed mapping are improved significantly over those without the mapping. Comparing to the homomorphic system, the proposed algorithm produces enhanced images with smaller distortions.

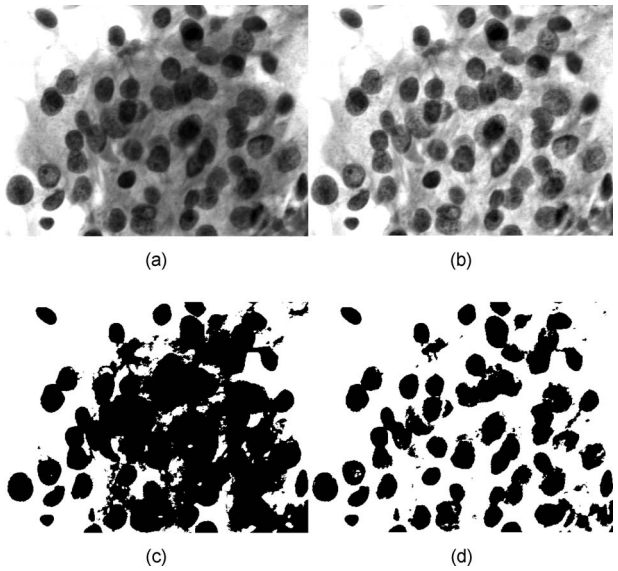

Figure 7. (a) Pancreatic ductal cell image; (b) envelope-mapping enhanced image; (c) automatic thresholding of image (a) at the middle of its intensity range; and (d) automatic thresholding of image (b) at the middle of its intensity range.

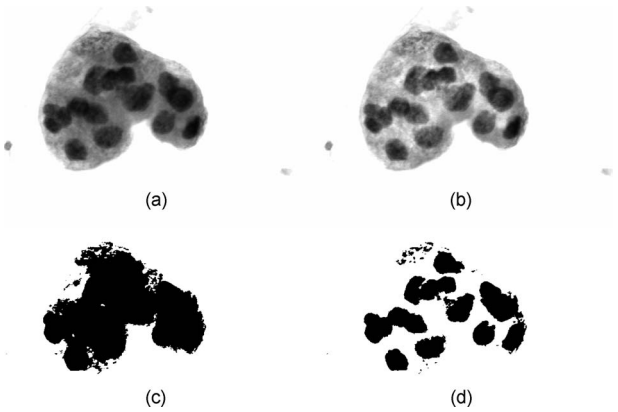

Figure 8. (a) Another pancreatic ductal cell image; (b) envelope-mapping enhanced image; (c) automatic thresholding of the image (a); and (d) automatic thresholding of the image (b).

REFERENCES

[1] R. M. DeMay, "Pancreas", *The Art and Science of Cytopathology* (American Society Clinical Pathologists, Chicago, 1996), Vol. II, pp. 1053–1082.

[2] D. M. McCarthy, A. Maitra, P. Argani, A. E. Rader, D. O. Faigel, N. T. Van Heek, R. H. Hruban, and R. E. Wilentz, "Novel markers of pancreatic adenocarcinoma in fine-needle aspiration: mesothelin and prostate stem cell antigen labeling increases accuracy in cytologically borderline cases", Appl. Immunohistochem Mol. Morphol. **11**, 238–243 (2003).

[3] M. Gao, P. Bridgman, and S. Kumara, "Computer aided prostate cancer diagnosis using image enhancement and JPEG2000", Proc. SPIE **5203**, 323–334 (2003).

[4] H.-S. Wu, A. J. Einstein, L. Deligdisch, T. Kalir, and J. Gil, "Characterization of nuclear images based on analysis of fractional summation systems", Fractals **12**, 1–13 (2004).

[5] T. Mattfeldt, H.-W. Gottfried, V. Schmidt, and H. A. Kestler, "Classification of spatial textures in benign and cancerous glandular tissues by stereology and stochastic geometry using artificial neural networks", J. Microsc. **198**, 143–158 (2000).

[6] U. Adiqa, R. Malladi, R. Fernandez-Gonzalez, and C. Ortiz de Solorzano, "High-throughput analysis of multispectral images of breast cancer tissue", IEEE Trans. Image Process. **15**, 2259–2268 (2006).
[7] H.-S. Wu and J. Gil, "Linear clustering for segmentation of color microscopic lung cell Images", J. Imaging Sci. Technol. **47**, 161–170 (2003).
[8] G. Begelman, E. Gur, E. Rivlin, M. Rudzsky, and Z. Zalevsky, "Cell nuclei segmentation using fuzzy logic engine", *Proc. Int. Conf. Image Proces.* (ICIP) (IEEE, Piscataway, NJ, 2004), Vol. **5**, pp. 2937–2940.
[9] D. Comaniciu, P. Meer, and D. J. Foran, "Image-guided decision support system for pathology", Mach. Vision Appl. **11**, 213–224 (1999).
[10] L. Yang, P. Meer, and D. J. Foran, "Unsupervised segmentation based on robust estimation and color active contour models", IEEE Trans. Inf. Technol. Biomed. **9**, 475–486 (2005).
[11] N. Malpica, C. Ortiz de Solorzano, J. J. Vaquero, A. Santos, I. Vallcorba, J. M. Garcia-Sagredo, and F. del Pozo, "Applying watershed algorithms to the segmentation of clustered nuclei", Cytometry **28**, 289–297 (1997).
[12] X. Chen, X. Zhou, and S. T. Wong, "Automated segmentation, classification, and tracking of cancer cell nuclei in time-lapse microscopy", IEEE Trans. Biomed. Eng. **53**, 762–766 (2006).
[13] H.-S. Wu, J. Barba, and J. Gil, "A parametric fitting algorithm for segmentation of cell images", IEEE Trans. Biomed. Eng. **45**, 400–407 (1998).
[14] E. Anguiano, M. Pancorbo, and M. Aguilar, "Fractal characterization by frequency analysis: I. surfaces", J. Microsc. **172**(3), 223–232 (1993).
[15] J. C. Russ, *The Image Processing Handbook*, 4th ed. (CRC Press, London, 2002).
[16] K. R. Castleman, *Digital Image Processing* (Prentice Hall, Englewood Cliffs, NJ, 1996).
[17] E. R. Dougherty, *An Introduction to Morphological Image Processing* (SPIE Optical Engineering Press, Bellingham, WA, 1992).
[18] N. Ahmed, T. Natarajan, and K. R. Rao, "Discrete cosine transform", IEEE Trans. Comput. **23**, 90–93 (1974).
[19] H.-S. Wu, "Hexagonal discrete cosine transform for image coding", Electron. Lett. **27**, 781–783 (1991).
[20] A. V. Oppenheim and R. W. Schafer, *Digital Signal Processing* (Prentice Hall, Englewood Cliffs, NJ, 1975).
[21] R. Kimmel, M. Elad, D. Shaked, R. Keshet, and I. Sobel, "A variational framework for retinex", Int. J. Comput. Vis. **52**, 7–23 (2003).